

# Batchelor, Saffman, and Kazantsev spectra in galactic small-scale dynamos

Axel Brandenburg<sup>1,2,3,4\*</sup>, Hongzhe Zhou<sup>1</sup>, and Ramkishor Sharma<sup>1,2</sup>

<sup>1</sup>*Nordita, KTH Royal Institute of Technology and Stockholm University, Hannes Alfvéns väg 12, SE-10691 Stockholm, Sweden*

<sup>2</sup>*The Oskar Klein Centre, Department of Astronomy, Stockholm University, AlbaNova, SE-10691 Stockholm, Sweden*

<sup>3</sup>*McWilliams Center for Cosmology and Department of Physics, Carnegie Mellon University, 5000 Forbes Ave, Pittsburgh, PA 15213, USA*

<sup>4</sup>*School of Natural Sciences and Medicine, Ilia State University, 3-5 Cholokashvili Avenue, 0194 Tbilisi, Georgia*

20 July 2022

## ABSTRACT

The magnetic fields in galaxy clusters and probably also in the interstellar medium are believed to be generated by a small-scale dynamo. Theoretically, during its kinematic stage, it is characterized by a Kazantsev spectrum, which peaks at the resistive scale. It is only slightly shallower than the Saffman spectrum that is expected for random and causally connected magnetic fields. Causally disconnected fields have the even steeper Batchelor spectrum. Here we show that all three spectra are present in the small-scale dynamo. During the kinematic stage, the Batchelor spectrum occurs on scales larger than the energy-carrying scale of the turbulence, and the Kazantsev spectrum on smaller scales within the inertial range of the turbulence – even for a magnetic Prandtl number of unity. In the saturated state, the dynamo develops a Saffman spectrum on large scales. At large magnetic Prandtl numbers, elongated structures are seen in the parity-even  $E$  polarization, but not in the parity-odd  $B$  polarization. We also observe a significant excess in the  $E$  polarization over the  $B$  polarization at subresistive scales, and a deficiency at larger scales. This finding is at odds with the observed excess in the Galactic microwave foreground emission. The  $E$  and  $B$  polarizations become Gaussian in the saturated state, but may be highly non-Gaussian and skewed in the kinematic regime of the dynamo.

**Key words:** dynamo – MHD – polarization – turbulence – galaxies: magnetic fields

## 1 INTRODUCTION

The possibility of small-scale magnetohydrodynamic (MHD) dynamos has been studied since the early work of Batchelor (1950), who assumed that the statistical properties of the magnetic field agree with those of vorticity. However, the nowadays accepted theory of small-scale dynamos was developed only later by Kazantsev (1968). However, the topic of small-scale dynamos moved somewhat into the background with the discovery of large-scale dynamos driven by the helicity or  $\alpha$  effect (Steenbeck et al. 1966; Moffatt 1978; Krause & Rädler 1980). With the advent of direct numerical simulations (DNS) of turbulence, the study of small-scale dynamos was picked up again by Meneguzzi et al. (1981) and Kida et al. (1991). In both studies, the addition of kinetic helicity had only a minor effect on the result, which was due to too small domain sizes. Early convection-driven dynamos with rotation (Meneguzzi & Pouquet 1989; Nordlund et al. 1992) therefore also essentially counted under this category. The work of Kazantsev (1968) became routinely quoted only since the 2000s when simulations began to reproduce what is nowadays often referred to as the Kazantsev spectrum (Schekochihin et al. 2004; Haugen et al. 2004).

The original theory of Kazantsev (1968) was linear, so it only described the early kinematic growth phase of the dynamo. Furthermore, it assumed that the velocity was smooth and of large scale only. In the framework of turbulence, this could be realized if the magnetic Prandtl number,  $\text{Pr}_M \equiv \nu/\eta$ , is large, i.e., if the viscosity

$\nu$  is much larger than the magnetic diffusivity  $\eta$ , making then the velocity field much smoother than the magnetic field. This situation is applicable to galaxies and galaxy clusters, but not to stars and other denser bodies.

Kazantsev’s theory yielded as the eigenfunction a magnetic energy spectrum  $E_M(k)$  proportional to  $k^{3/2}K_0(k/k_\eta)$ , where  $k$  is the wavenumber,  $K_0$  is the Macdonald function of order zero or the modified Bessel function of the second kind, and  $k_\eta = (2\pi\gamma/5\eta)^{1/2}$  is the resistive cutoff wavenumber (Kulsrud & Anderson 1992) with  $\gamma$  being the growth rate. Such scaling was indeed confirmed in a number of different DNS (Schekochihin et al. 2004; Haugen et al. 2004). However, it is important to recall that this scaling is only expected for large values of  $\text{Pr}_M$ . In the opposite limit of  $\text{Pr}_M \ll 1$ , the spectral slope may be smaller. Brandenburg et al. (2018) confirmed a  $k^{7/6}$  scaling for  $\text{Pr}_M = 0.1$ , as was previously discussed by Subramanian & Brandenburg (2014).

In the meantime, there has been a significant amount of work on decaying turbulence. Much of this was motivated by applications to the early universe (Brandenburg et al. 1996; Christensson et al. 2001; Banerjee & Jedamzik 2004). An important question here is how rapidly the magnetic energy decays and how rapidly the correlation length of the turbulence increases. It has been argued that this may depend on the slope of the subinertial range spectrum, i.e., on the exponent  $\alpha$  in the magnetic energy spectrum  $E_M(k) \propto k^\alpha$ . Here, the subinertial range is the low wavenumber part of the spectrum below the peak wavenumber (Olesen 1997). Above the peak, we usually have the inertial range, where the velocity is expected to

\* E-mail: brandenb@nordita.org

have a Kolmogorov  $k^{-5/3}$  spectrum, which is followed by the viscous subrange above some viscous cutoff wavenumber.

Olesen (1997) found the possibility of inverse cascading, i.e., a temporal increase of the spectral power for small  $k$  and a rapid decrease of the correlation length  $\xi_M$  when  $\alpha$  is large enough. The inverse correlation length  $\xi_M^{-1}$  is usually close to the position of the peak of the spectrum of  $E_M(k)$ . In forced turbulence, we have  $\xi_M^{-1} \approx k_f$ , where  $k_f$  is the forcing wavenumber, but in decaying turbulence, its value is time-dependent (and decreasing).

In the simulations of Christensson et al. (2001), an initial  $k^4$  spectrum was assumed. The value  $\alpha = 4$  was argued to be a general consequence of the requirement of causality in the early Universe, i.e., the requirement that the magnetic field  $\mathbf{B}$  is uncorrelated over different positions, and the fact that  $\nabla \cdot \mathbf{B} = 0$  (Durrer & Caprini 2003). A  $k^4$  subinertial range spectrum is usually referred to as a Batchelor spectrum. DNS have shown that, in the presence of magnetic helicity, a  $k^4$  spectrum develops automatically, even when the initial spectrum was shallower, e.g.,  $\propto k^2$ , which is called a Saffman spectrum in hydrodynamic turbulence without helicity (Saffman 1967). However, subsequent work showed that this is only true because of the presence of magnetic helicity and that, then, non-helical turbulence with an initial Saffman spectrum preserves its initial  $k^2$  slope (Reppin & Banerjee 2017; Brandenburg et al. 2017).

Many of the MHD decay studies were done for magnetically dominated turbulence (Brandenburg et al. 2015; Brandenburg & Kahniashvili 2017), i.e., the initial magnetic energy density is large compared with the kinetic energy density of the turbulence. This precludes the investigation of dynamo action, i.e., the conversion of kinetic energy into magnetic. Simulations of Brandenburg et al. (2019a) showed that a nearly exponential increase of magnetic energy is still possible for some period of time when the initial magnetic energy density is small enough.

To summarize, in decaying MHD turbulence, the magnetic energy spectrum can have a  $k^2$  or a  $k^4$  spectrum (see the discussion in Sect. 3.5 of Subramanian 2019), depending on the initial conditions. For nonhelical turbulence, in particular, there is no reason to expect a  $k^4$  spectrum, unless the causality argument of Durrer & Caprini (2003) can be invoked. Earlier work did show a  $k^4$  spectrum of the magnetic field in the kinetically dominated case; see Figure 8 of Brandenburg et al. (2019a), but this was in the presence of helicity. Moreover, there was no indication of a Kazantsev  $k^{3/2}$  spectrum. This could perhaps be related to the fact that in those simulations, the magnetic Prandtl number was chosen to be unity, i.e., not  $\gg 1$ . There remained therefore the question, how the Batchelor  $k^4$  spectrum, the Saffman  $k^2$  spectrum, and the Kazantsev  $k^{3/2}$  spectrum are related to each other. Disentangling this is the motivating topic of this paper.

We consider forced turbulence with a weak initial seed magnetic field. We consider DNS with a resolution of  $N^3 = 1024^3$  mesh points, which is still not large enough to cover all turbulent subranges in one simulation, but experimenting with selected subranges remains affordable. We therefore compare simulations with different values of  $\text{Pr}_M$  and  $k_f$ . It will turn out that all three spectra, the Batchelor, Saffman, and Kazantsev spectra are being realized in the small-scale dynamo problem if the range of available wavenumbers is large enough; the Batchelor and Saffman spectra are being found in the subinertial range during the kinematic and saturated growth phases, respectively, and the Kazantsev  $k^{3/2}$  spectrum is found in what corresponds to the magnetic inertial range during the kinematic phase. In the saturated stage, however, it changes to a declining spectrum, which is typically close to the Kolmogorov  $k^{-5/3}$  spectrum, or the Iroshnikov-Kraichnan  $k^{-3/2}$  slope, whose theoretical foundation is still subject to research (Boldyrev 2005, 2006; Schekochihin 2020).

We complete our study with a comparison of different diagnostic quantities. Specifically, we estimate the rotation measure (RM) and the parity-even and parity-odd linear polarizations,  $E$  and  $B$ , respectively. The latter two are routinely used in cosmology and nowadays also in connection with investigations of the interstellar medium (ISM; see the Planck Collaboration et al. 2016).

## 2 OUR MODEL

### 2.1 Basic equations

We consider weakly compressible turbulence with an isothermal equation of state and constant speed of sound  $c_s$ , where the pressure  $p$  is proportional to the density  $\rho$ , i.e.,  $p = \rho c_s^2$ . We solve for the magnetic vector potential  $\mathbf{A}$ , so the magnetic field is  $\mathbf{B} = \nabla \times \mathbf{A}$ . The full set of evolution equations for  $\mathbf{A}$ , the velocity  $\mathbf{U}$ , and the logarithmic density  $\ln \rho$  is given by

$$\frac{\partial \mathbf{A}}{\partial t} = \mathbf{u} \times \mathbf{B} + \eta \nabla^2 \mathbf{A}, \quad (1)$$

$$\frac{D\mathbf{u}}{Dt} = \mathbf{f} - c_s^2 \nabla \ln \rho + \frac{1}{\rho} [\mathbf{J} \times \mathbf{B} + \nabla \cdot (2\rho \mathbf{vS})], \quad (2)$$

$$\frac{D \ln \rho}{Dt} = -\nabla \cdot \mathbf{u}, \quad (3)$$

where  $\mathbf{J} = \nabla \times \mathbf{B} / \mu_0$  is the current density and  $\mu_0$  is the vacuum permeability,  $S_{ij} = (\partial_i u_j + \partial_j u_i) / 2 - \delta_{ij} \nabla \cdot \mathbf{u} / 3$  are the components of the rate-of-strain tensor  $\mathbf{S}$ , and  $\mathbf{f}$  is a nonhelical forcing function consisting of plane waves with wavevector  $\mathbf{k}$ . It is proportional to  $(\hat{\mathbf{e}} \times \mathbf{k}) e^{i\mathbf{k} \cdot \mathbf{x}}$ , where  $\mathbf{x}$  is position and  $\hat{\mathbf{e}}$  is a randomly chosen unit vector that is not aligned with  $\mathbf{k}$ . The wavevector  $\mathbf{k}$  changes randomly at each time step, making the forcing function therefore  $\delta$  correlated in time. We select the wavevectors  $\mathbf{k}$  randomly from a finite set of vectors whose components are multiples of  $k_1 \equiv 2\pi/L$ , where  $L$  is the side length of our Cartesian domain of volume  $L^3$ . This forcing function has been used in many earlier papers (e.g. Haugen et al. 2004).

### 2.2 Governing parameters and diagnostics

For all our simulations, we use the PENCIL CODE (Pencil Code Collaboration et al. 2021), which is an explicit code whose time step is given by the Courant-Friedrich-Lewy condition and therefore scales inversely with the maximum wave speed. We arrange the forcing strength such that the Mach number based on the rms velocity of the turbulence,  $\text{Ma} = u_{\text{rms}} / c_s$ , is around 0.1. This choice ensures that the turbulence is sufficiently subsonic and therefore close to the incompressible limit, but not so small that the sound speed, which is the main factor limiting the time step, does not exceed  $u_{\text{rms}}$  by an unreasonably large amount.

Our governing parameters are the fluid and magnetic Reynolds numbers, defined here as

$$\text{Re} = u_{\text{rms}} / \nu k_f, \quad \text{Re}_M = u_{\text{rms}} / \eta k_f, \quad (4)$$

respectively. Thus,  $\text{Pr}_M = \text{Re}_M / \text{Re}$ . We usually try to keep these two Reynolds numbers as large as possible. As a rule of thumb, one may say that the product of  $(k_f / k_1) \times \max(\text{Re}, \text{Re}_M)$  should not exceed the mesh size by a large factor. Usually, the simulation would “crash”, i.e., the turbulent energy cannot be dissipated anymore at the highest wavenumbers. Even if the simulation does not crash, the accuracy

of the results may be affected. However, since potential artifacts are expected to affect mostly the high wavenumber part of the spectrum, we might still trust the low wavenumber part. It should be kept in mind that a small Reynolds number also causes artifacts, because the simulation becomes too diffusive, so it is essential to choose just the right value. This can only be decided in the context of and through the comparison with simulations for other parameters.

In any dynamo problem, an important output parameter is the growth rate

$$\gamma = \langle d \ln B_{\text{rms}}/dt \rangle_{\text{kin}}, \quad (5)$$

where the subscript ‘kin’ denotes a time average over the kinematic stage. We normalize  $\gamma$  by the turnover rate and denote it by a tilde, i.e.,  $\tilde{\gamma} = \gamma/u_{\text{rms}}k_f$ , where  $u_{\text{rms}}$  is taken from the kinematic phase of the dynamo.

We define kinetic and magnetic energy spectra that are normalized such that  $\int E_K(k) dk = \langle \mathbf{u}^2 \rangle / 2$  and  $\int E_M(k) dk = \langle \mathbf{B}^2 \rangle / 2\mu_0\rho_0$ , respectively, where  $\rho_0$  is the mean density. Here, angle brackets without subscript denote volume averages. Note that the integrals over our energy spectra have units of energy per unit mass. We always present time-averaged spectra, which is straightforward for the kinetic energy because they are statistically stationary, and it is therefore also straightforward for the magnetic energy in the saturated regime, but in the kinematic phase,  $E_M(k, t)$  is exponentially growing with the rate  $2\gamma$ , so we average the compensated spectra,  $\langle e^{-2\gamma t} E_M(k, t) \rangle_{\text{kin}}$ , over a suitable time interval where the product is stationary; see also [Subramanian & Brandenburg \(2014\)](#) where this was done.

When plotting spectra, we normalize  $k$  by the viscous dissipation wavenumber

$$k_v = (\epsilon_K/\nu^3)^{1/4}, \quad (6)$$

where  $\epsilon_K = \langle 2\rho\nu\mathbf{S}^2 \rangle$  is the kinetic energy dissipation rate. Furthermore, one would often present compensated spectra by normalizing them with  $k^{5/3}\epsilon_K^{-2/3}$ , which would not only make it nondimensional, but this would then also yield a flat inertial range, whose mean value,  $\langle E_K(k) k^{5/3} \epsilon_K^{-2/3} \rangle_{\text{inert}} \equiv C_{\text{Kol}}$  would yield the Kolmogorov constant,  $C_{\text{Kol}}$ , and the subscript ‘inert’ denotes averaging over the inertial subrange. Here, we are not so much interested in the inertial range and would instead like the original slopes to be persevered. Therefore, we normalize with a  $k$ -independent, fixed value  $k_f^{5/3}\epsilon_K^{-2/3}$ , which would still allow us to read off the approximate Kolmogorov constant at the position of the peak of the spectrum normalized in this way.

We select forcing wavevectors  $\mathbf{k}$  from a narrow band of vectors with  $k_f - \delta k/2 \leq |\mathbf{k}| < k_f + \delta k/2$ , where  $\delta k$  is chosen such that the number of possible wavevectors does not exceed 10,000. For large values of  $k_f/k_1$ , we therefore reduce  $\delta k$ . This manifests itself in the kinetic energy of spectra, which then have a progressively sharper spike as the forcing wavenumber is increased.

### 3 RESULTS ON THE ENERGY SPECTRA

#### 3.1 Presentation of the results

We summarize our simulations in Table 1. Here, the runs are listed in the order of decreasing  $k_f$  and increasing Re. Again, the tildes denote normalized quantities, i.e.,  $\tilde{k}_f = k_f/k_1$ ,  $\tilde{k}_v = k_v/k_1$ ,  $\tilde{v}_A^{\text{rms}} = v_A^{\text{rms}}/c_s$ , where  $v_A^{\text{rms}} = B_{\text{rms}}/\sqrt{\mu_0\rho_0}$  is used to quantify the magnetic field strength as an Alfvén velocity. The values of  $\tilde{v}_A^{\text{rms}}$  refer to the saturated state, but all others refer to the kinematic phase. During saturation, Ma decreases, especially when  $\text{Pr}_M = 1$ ; see Appendix A for details.

**Table 1.** Summary of the simulations presented in this paper.

Run	Ma	$\tilde{k}_f$	$\tilde{k}_v$	$\tilde{\gamma}$	$\tilde{v}_A^{\text{rms}}$	Re	$\text{Re}_M$	$\text{Pr}_M$
A	0.111	120	764	0.022	0.01	31	31	1
B	0.121	30	389	0.027	0.03	81	81	1
C	0.118	10	106	0.085	...	59	590	10
D	0.122	4	62	0.130	0.08	100	3000	30
E	0.130	4	461	0.158	0.10	1600	1600	1

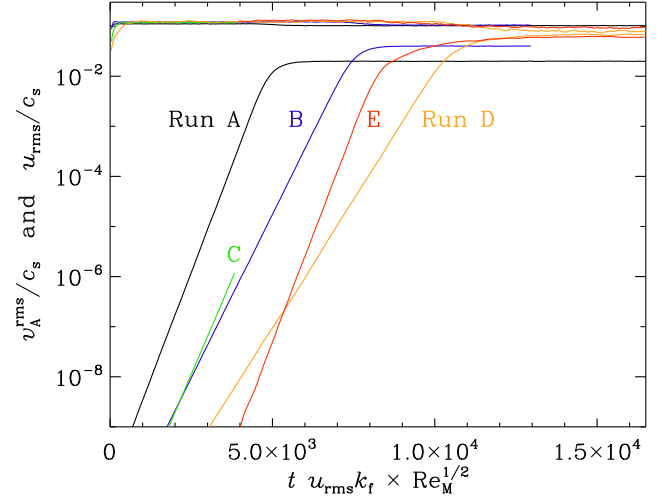


**Figure 1.** Time series of  $u_{\text{rms}}$  and  $v_A^{\text{rms}} = B_{\text{rms}}/\sqrt{\mu_0\rho_0}$ , normalized by  $c_s$ .

We begin by discussing Run B with  $\text{Pr}_M = 1$  and then Runs C and D with  $\text{Pr}_M = 10$  and  $30$ . The reason we discuss Run A with  $k_f/k_1 = 120$  later is because we first want to motivate the need for going to such an extremely high value of  $k_f$ . Finally, we present with Run E a case where  $\text{Pr}_M = 1$ , so as to show that the choice of large magnetic Prandtl numbers is not necessary to obtain a Kazantsev spectrum in the kinematic phase. For all runs, the evolution of  $u_{\text{rms}}$  and  $B_{\text{rms}}$  is shown in Fig. 1. Here, the time axis is normalized by the turnover time,  $1/u_{\text{rms}}k_f$ , and scaled by the square root of the Reynolds number, so as to have comparable saturation times.

#### 3.2 Subinertial range during saturation

To begin with, we consider a case with  $\text{Pr}_M = 1$  and  $k_f/k_1 = 30$ ; see Fig. 2. For this and the following spectra, we have fixed the ranges on the abscissa and ordinate so as to facilitate comparison between them. The position of the peak of the spectrum is clearly visible as a sharp spike, as explained in Sect. 2.2. We see that during the kinematic and saturated phases of the dynamo, indicated by dashed and solid lines, respectively, the kinetic energy spectrum always has a clear  $k^2$  subinertial range, while the magnetic field has a steeper subinertial range during the kinematic growth phase (closer to  $k^3$ ), but becomes proportional to  $k^2$  during the saturated phase.

We note that there is no Kazantsev  $k^{3/2}$  slope in the kinematic range. This may have two reasons:  $\text{Pr}_M$  is not large enough or the turbulent inertial range is too short. Therefore, we consider next a run with larger values of  $\text{Pr}_M$ . Later we also reconsider runs with  $\text{Pr}_M = 1$  using both a larger and a smaller value of  $k_f$ .

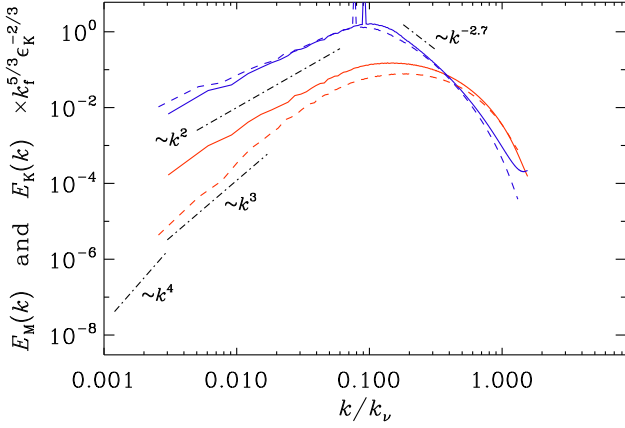


**Figure 2.** Kinetic (blue) and magnetic (red) energy spectra for Run B during the kinematic (dotted lines) and the saturated (solid lines) stages.

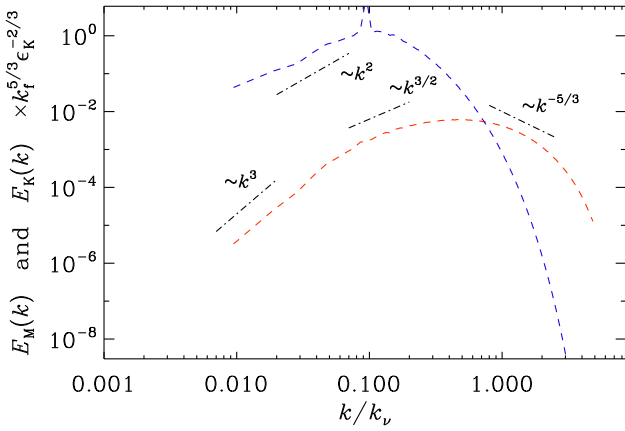


**Figure 3.** Similar to Fig. 2, but for Run C, except that the spectra are only shown for the kinematic phase.

### 3.3 Emergence of the Kazantsev slope

We now consider Runs C and D with larger magnetic Prandtl numbers,  $\text{Pr}_M = 10$  and  $30$ , respectively. Of these two runs, only Run D has been run into saturation, because we expect their nonlinear behaviors to be similar. In these runs, shown in Figs. 3 and 4, we also decrease the value of  $k_f$  to  $10$  and  $4$ , respectively. In both cases, we clearly see the emergence of a Kazantsev  $k^{3/2}$  subrange for  $k > k_f$ . For Run D, we also see that the Kazantsev slope disappears in the saturated state. We still see in the kinematic phase the  $k^3$  subrange for  $k < k_f$ . However, it is possible that the actual slope of the kinematic subrange spectrum is steeper, and that we just did not have enough scale separation between the lowest wavenumber  $k_1$  and the forcing wavenumber  $k_f$ . Therefore, we now consider a more extreme case with even more scale separation.

### 3.4 Batchelor spectrum in the kinematic stage

To see whether the  $k^3$  subrange slope found in Sect. 3.2 was a consequence of still insufficient scale separation, we now consider a more extreme case with a four times larger value, namely  $k_f/k_1 = 120$ ; see Fig. 5. We now see that there is indeed a  $k^4$  Batchelor subinertial range. Interestingly, we also see that near the very lowest

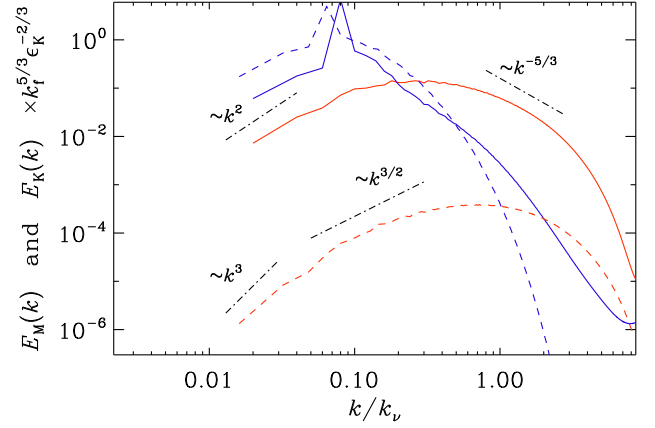


**Figure 4.** Similar to Fig. 2, but for Run D.

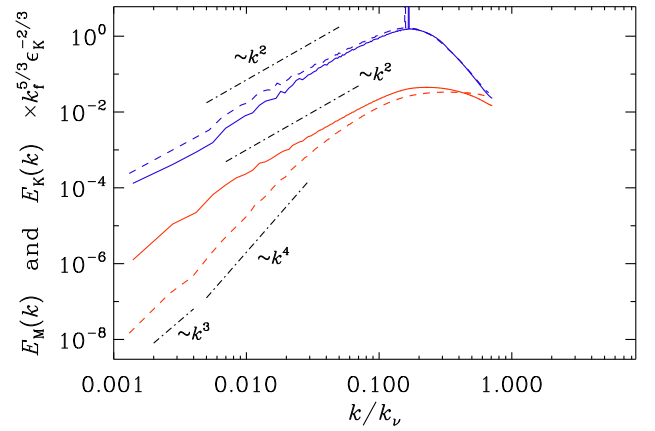


**Figure 5.** Similar to Fig. 2, but for Run A. Note the  $k^4$  subrange of  $E_M(k)$  in the kinematic stage, but also evidence for slight contamination at very small  $k$ .

wavenumbers in the domain, the spectrum does become slightly shallower. This suggests that the spectrum at those low wavenumbers,  $1 \leq k/k_1 \leq 3$ , is indeed contaminated by finite size effects of the computational domain.

To demonstrate that the  $k^4$  subrange existed throughout the entire kinematic phase, we show in Fig. 6 unnormalized spectra for Run A in regular time intervals during the kinematic stage and less frequently during the saturated stage, where the low wavenumber part is seen to grow slightly. The final slope during the saturated stages is  $\propto k^2$ , just like the kinetic energy spectrum; see Fig. 5.

### 3.5 Kazantsev spectrum at $\text{Pr}_M = 1$

We recall that, in order to see the Kazantsev spectrum, we increased  $\text{Pr}_M$  from one to  $10$  and  $30$ , but we also decreased  $k_f/k_1$  from  $30$  to  $10$  and  $4$ . We now show that a larger value of  $\text{Pr}_M$  was helpful in achieving dynamo action, but it was not essential for obtaining the Kazantsev spectrum. The important point is rather that the Kazantsev spectrum is really an inertial range phenomenon and is not present in the subinertial range. Therefore, all that is required is a long enough inertial range. To show this more clearly, we now present a case with  $\text{Pr}_M = 1$  and  $k_f/k_1 = 4$ ; see Fig. 7. Here, we now clearly see the Kazantsev spectrum during the kinematic stage of the dynamo.



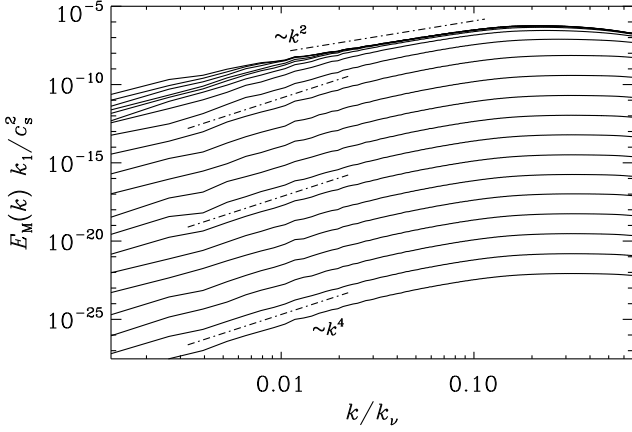


**Figure 6.** Unnormalized spectra for Run A showing that the  $k^4$  subrange existed throughout the entire kinematic phase.

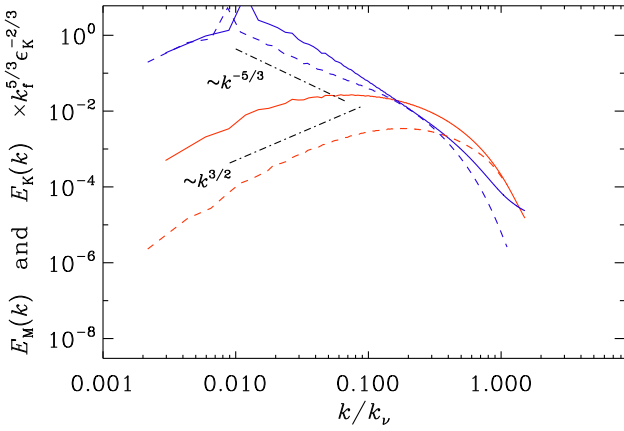


**Figure 7.** Similar to Fig. 2, but for Run E. Note the well developed  $k^{3/2}$  Kazantsev slope for  $E_M(k)$  during the kinematic stage in the range where  $E_K(k)$  shows a  $k^{-5/3}$  Kolmogorov subrange with bottleneck in the kinematic stage.

In Fig. 7, we see that, in the wavenumber interval with the Kazantsev slope in the magnetic energy spectrum, we also have a Kolmogorov inertial range in the kinetic energy spectrum together with a slight uprise near the dissipation wavenumber. This uprise is well known in turbulence theory and is referred to as the bottleneck effect (Falkovich 1994). It is a phenomenon that is particularly clear in the three-dimensional spectra presented here, but it is less pronounced in the one-dimensional spectra considered in observations such as wind tunnel experiment, which has a simple mathematical reason (Dobler et al. 2003). This leads us now to the next section where we consider diagnostic aspects in determining different slopes observationally.

## 4 DIAGNOSTICS OF DIFFERENT SUBRANGES

### 4.1 Synchrotron emission and $E$ and $B$ polarization

In the ISM, one can measure the magnetic field through linearly polarized synchrotron emission. The Stokes  $Q$  and  $U$  parameters can be combined with into a complex polarization  $P = Q + iU$ , which is

**Table 2.** Diagnostic properties of Runs A–E. In some cases, the values for the saturated state are given in the second row for that run.

Run	$q_{LS}$	$q_{SS}$	elong. struct. in $E$	spectra
A	0.84	1.41	no; random	Batchelor
	0.87	1.18	no; random	Saffman
B	0.66	3.3	marginal	$k^3$ and Saffman
	0.68	6.4	marginally	$k^2$
C	0.42	4.6	weakly	$k^3$ and short Kaz.
D	0.37	5.7	very clear	$k^4$ and Kazantsev
	0.57	16	yes, but larger scale	$k^2$ and flat part
E	0.63	3.0	somewhat	clear Kazantsev
	0.82	70	yes, but larger scale	nearly flat

given by a line-of-sight integration (Pacholczyk 1970),

$$P = - \int_0^\infty \epsilon_0 \mathcal{B}^2 e^{2i\phi(z)\lambda^2} dz, \quad (7)$$

where  $\epsilon_0$  quantifies the emissivity, which is here taken as a constant,  $\mathcal{B} = B_x + iB_y$  is the complex magnetic field in the observational plane, and  $\phi = -K \int_0^z n_e B_z dz'$  is the Faraday depth with  $n_e$  being the density of thermal electrons and  $K$  is a constant. The Faraday depth across a slab of length  $L$  is  $\phi(L)$  and gives the rotation measure as  $RM = \phi(L)/2$  (Brandenburg & Stepanov 2014). Observationally, RM can be determined by varying the radio wavelength  $\lambda$ , i.e.,  $RM = d \arg(P)/d\lambda^2$ , where  $\arg(P)$  is the phase of  $P$ . If the electron density is approximately constant, RM is proportional to the line-of-sight integrated line-of-sight component of the magnetic field. Significant amount of work has been done to establish the relation between the spectra of the magnetic field and those of RM (Cho & Ryu 2009; Bhat & Subramanian 2013; Sur et al. 2018; Seta et al. 2022).

As observational diagnostics, we present the line-of-sight averaged magnetic field,  $\langle B_z \rangle_z(x, y)$ , as a proxy for RM when  $n_e = \text{const}$ , and the linear polarization  $P(x, y)$  in the absence of Faraday depolarization, i.e.,  $\lambda = 0$ . In the following, however, we convert  $P(x, y)$  into the parity-even and parity-odd  $E$  and  $B$  polarizations by computing (Seljak & Zaldarriaga 1997; Kamionkowski et al. 1997; Brandenburg et al. 2019b)

$$R(x, y) = \mathcal{F}^{-1} \left[ (k_x - ik_y)^2 \mathcal{F}(P) \right], \quad (8)$$

where  $\mathcal{F}(P) = \int P(\mathbf{x}_\perp) e^{i\mathbf{k}_\perp \cdot \mathbf{x}_\perp} d^2\mathbf{x}_\perp / (2\pi)^2$  is a function of  $\mathbf{k}_\perp \equiv (k_x, k_y)$  and denotes the Fourier transformation over the  $\mathbf{x}_\perp \equiv (x, y)$  plane, and  $\mathcal{F}^{-1}$  denotes the inverse transformation. The real and imaginary parts of  $R(x, y)$  give the parity-even and parity-odd  $E$  and  $B$  polarizations, respectively.

### 4.2 Diagnostic images and spectra

In Fig. 8, we present images of  $E(x, y)$ ,  $B(x, y)$ , and  $\langle B_z \rangle_z(x, y)$ , where the latter will simply be denoted by RM. The structures are rather small, so we also show an enlarged presentation of  $1/8^2$  of the image, as indicated by the white box on the corresponding full images.

Next, we present diagnostic spectra from our two-dimensional images for Run E during the kinematic stage. They are denoted by  $\text{Sp}(E)$ ,  $\text{Sp}(B)$ , and  $\text{Sp}(\text{RM})$  and are normalized such that  $\int \text{Sp}(\text{RM}) dk = 1$  and  $\int [\text{Sp}(E) + \text{Sp}(B)] dk = 1$ ; see Fig. 9. For comparison, we also overplot  $E_M(k)/k$ , suitably normalized, which is seen to agree with  $\text{Sp}(\text{RM})$ . It turns out that in  $0.01 \leq k/k_v \leq 0.1$ ,  $\text{Sp}(\text{RM})$  and  $\text{Sp}(E)$  are proportional to  $k^{1/2}$ . On the other hand,

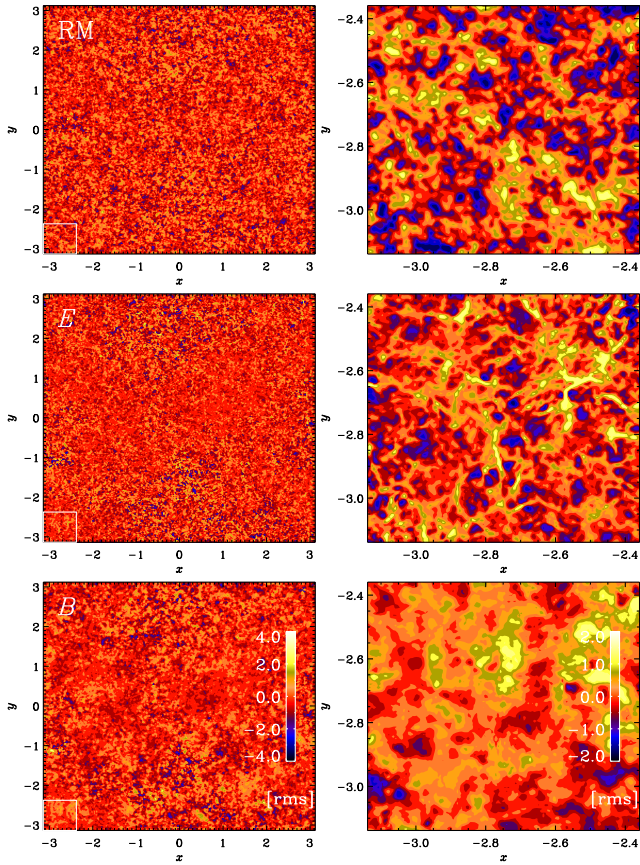


**Figure 8.** Diagnostic slices of RM (top row),  $E$  (middle row), and  $B$  (bottom row), for Run E during the kinematic stage. The small white squares on the left column mark the part that is shown enlarged on the right column. All quantities are normalized by their rms value and the color bars for the enlarged frames are clipped at  $\pm 2$  times the rms value, while those for the full frames are clipped at  $\pm 4$  times the rms value.

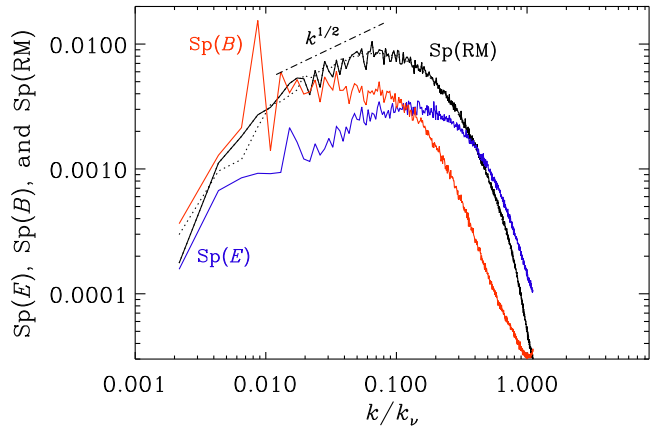


**Figure 9.** Diagnostic spectra  $Sp(E)$  (blue line),  $Sp(B)$  (red line), and  $Sp(RM)$  (black line) for Run E during the kinematic stage. The dotted line gives  $E_M(k)/k$ , normalized so that it nearly overlaps with  $Sp(RM)$ .

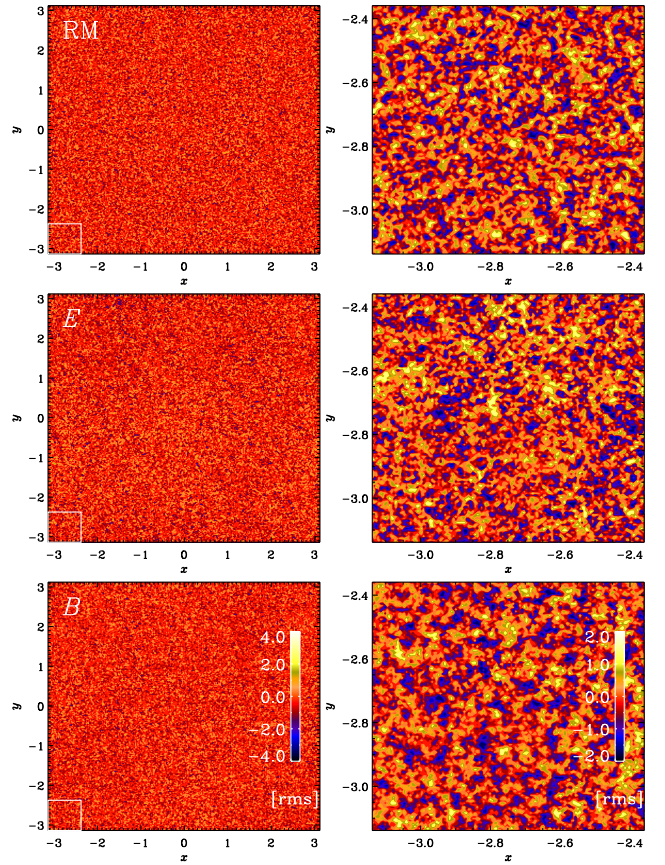


**Figure 10.** Same as Fig. 8, but for Run A during the kinematic stage.

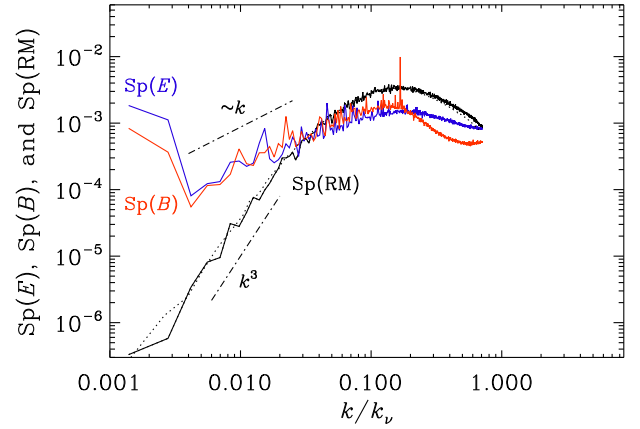


**Figure 11.** Same as Fig. 9, but for Run A during the kinematic stage.

$Sp(B)$  is flat; see Table 3 for the approximate wavenumber scalings of  $E_M(k)$ ,  $Sp(RM)$ ,  $Sp(E)$ , and  $Sp(B)$  for the inertial range of Run E.

For white noise in two dimensions, we would expect a linearly increasing spectrum. In the present case, this is indeed the case for the  $E$  and  $B$  polarizations in the subinertial range of Run A; see Table 2 and Figs. 10 and 11.

The correspondence between the exponent  $\alpha$  in  $E_M(k) \propto k^\alpha$  and  $\alpha_{RM}$  in  $Sp(RM) \propto k^{\alpha_{RM}}$  with  $\alpha_{RM} = \alpha - 1$  is explained by the line-of-sight integration, which removes the spatial dependence in one direction. For Run E, this is also seen for  $\alpha_E$  in  $Sp(E) \propto k^{\alpha_E}$



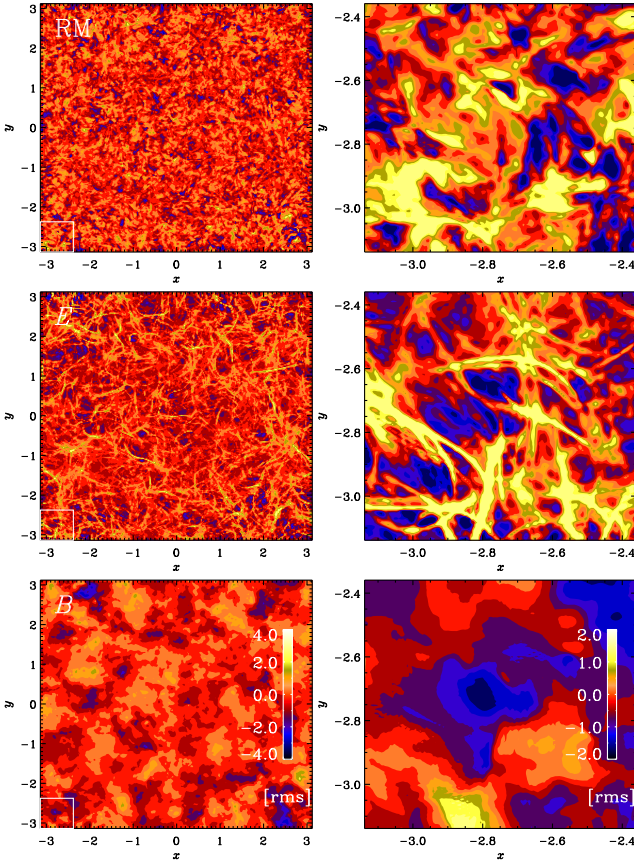


Figure 12. Same as Fig. 8, but for Run D during the kinematic stage.

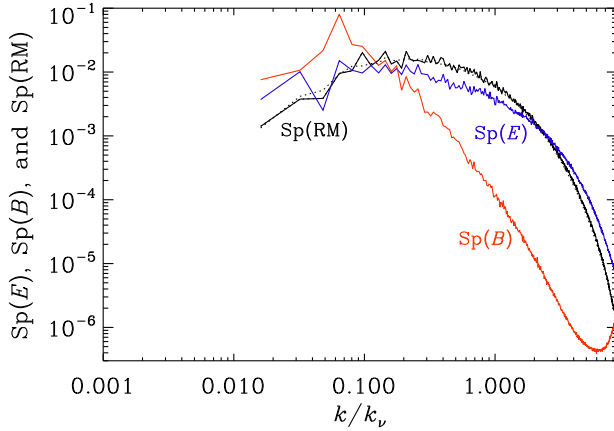


Figure 13. Same as Fig. 9, but for Run D during the kinematic stage.

**Table 3.** Approximate wavenumber scalings of  $E_M(k)$ ,  $Sp(RM)$ ,  $Sp(E)$ , and  $Sp(B)$  for the subinertial range of Run A and the inertial range of Run E.

Run	range	$E_M(k)$	$Sp(RM)$	$Sp(E)$	$Sp(B)$
A	subinertial	$k^4$	$k^3$	$k^1$	$k^1$
E	inertial	$k^{3/2}$	$k^{1/2}$	$k^{1/2}$	$k^0$

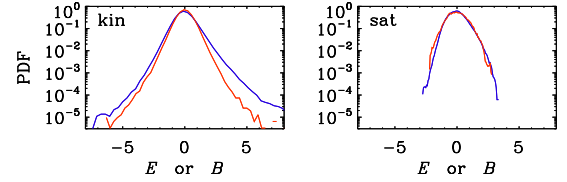


Figure 14. PDFs of  $E$  (blue lines) and  $B$  (red lines) during the kinematic (left) and saturated (right) stages for Run E.

with  $\alpha_E = \alpha - 1$ . As already alluded to above, here, and also in the runs with a Kazantsev spectrum in the inertial range,  $Sp(B)$  shows a marked decline with  $k$ . It is surprising to have such a strong difference in the spectral properties between  $E$  and  $B$ . This is probably explained by the mutual cancelation of opposite parities along the line of sight, which can only affect the parity-odd  $B$  polarization, and would have been missed if one just looked at the Stokes  $Q$  and  $U$  polarizations.

It is interesting to note that  $Sp(B)$  shows a strong decline near  $k/k_\nu = 0.1$ , and it also shows a peak at  $k_f$ . This suggests that the  $B$  polarization reflects properties of the velocity field. The strong decline of  $Sp(B)$  toward large  $k$  could therefore be a signature of the viscous cutoff.

One might have expected that the  $E$  and  $B$  spectra, which are quadratic in the magnetic field, have their peak at twice the wavenumber of the magnetic field spectra. This expectation was motivated by the fact that magnetic stress spectra occur at twice the peak wavenumber of the magnetic field itself (Brandenburg & Boldyrev 2020). In particular, the peak of  $Sp(B^2)$  is twice that of  $Sp(B)$ . This is not really seen in the present runs. Investigating the theoretical relations between the spectra of  $\mathcal{B}$  and  $\mathcal{B}^2$ , for example, is clearly of interest, but beyond the scope of the present paper.

For Run D, which has a large magnetic Prandtl number, we see very pronounced elongated structures in the  $E$  polarization, which is not seen in the  $B$  polarization, and only to some extent in RM; see Fig. 12. This corresponds with the spectra shown in Fig. 13, where  $Sp(RM)$  and  $Sp(E)$  have a similar shape, but  $Sp(B)$  shows a sharp decline with increasing  $k$ .

As expected, the corresponding visualizations for Run A show much smaller structures (see Fig. 10), but now the  $E$  and  $B$  polarization spectra are similar to each other, while the RM spectrum is much steeper; see Fig. 11. This is consistent with the expectations for random magnetic fields.

### 4.3 Excess $E$ polarization in statistics

Of particular interest is the ratio  $\langle E^2 \rangle / \langle B^2 \rangle$ . As we saw from Fig. 9, the answer may depend on the wavenumber range for which the data is taken. For Runs D and E, the  $E$  and  $B$  spectra cross, and the crossing point  $k_\times$  of the  $E$  and  $B$  spectra lies at  $k_\times/k_\nu \approx 0.14$ . It is therefore useful to compute the ratio separately for small and large  $k$ .

$$q_{LS} \equiv \langle E^2 \rangle_{LS} / \langle B^2 \rangle_{LS} = \int_0^{k_\times} Sp(E) dk \Big/ \int_0^{k_\times} Sp(B) dk, \quad (9)$$

$$q_{SS} \equiv \langle E^2 \rangle_{SS} / \langle B^2 \rangle_{SS} = \int_{k_\times}^\infty Sp(E) dk \Big/ \int_{k_\times}^\infty Sp(B) dk, \quad (10)$$

The resulting ratios are listed in Table 2, along with other observations about the runs.

Earlier work on the  $E$  and  $B$  polarizations has shown a tendency for the probability functions (PDFs) of  $E$  to be non-Gaussian

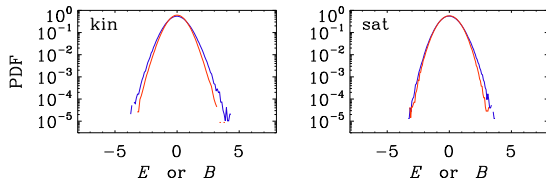


Figure 15. Same as Fig. 14, but for Run A.

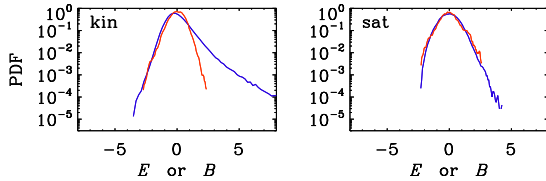


Figure 16. Same as Fig. 14, but for Run D.

Table 4. Skewness and kurtosis for our runs during the kinematic and saturated stages.

Run	skew( $E$ )	skew( $B$ )	kurt( $E$ )	kurt( $B$ )
A	0.05	0.00	0.20	0.17
	0.06	-0.00	0.05	-0.07
B	0.36	0.02	0.88	0.34
	0.19	-0.00	0.20	0.03
C	1.18	0.03	5.94	0.41
	1.53	-0.20	7.66	0.39
D	0.17	0.26	0.18	0.62
	0.51	0.00	4.23	3.37
E	0.40	0.17	0.38	-0.02

and skewed, while the  $B$  polarization was more nearly Gaussian (Brandenburg et al. 2019b; Brandenburg 2019), especially in decaying turbulence. In the present case, the result depends on the existence of an inertial range (Run E) and on whether the run is saturated or not. In Fig. 14 we show that for Run E, the PDFs correspond to stretched exponentials during the kinematic stage, with  $E$  being also skewed, but both become nearly Gaussian during the saturated stage. For Run A, on the other hand,  $E$  and  $B$  are nearly Gaussian both during the kinematic and the saturated stages; see Fig. 15. Run D is closer to Run E than to Run A, but with the  $E$  polarization being even more skewed during the kinematic stage; see Fig. 16. This could be a signature of the large magnetic Prandtl number in this case. In Table 4, we summarize the resulting values for skewness and kurtosis for all runs during the kinematic and saturated stages. Both the kurtosis and the skewness are particularly high for the runs with large magnetic Prandtl number (Runs C and D) during the kinematic phase. For Run E, the kurtosis of  $E$  is also fairly large during the kinematic phase, but the skewness is now only 0.5. For this run, furthermore, even the kurtosis of  $B$  is significant.

For completeness, we present images and spectra of  $E$ ,  $B$ , and RM for the other runs in Appendix B. The magnetic field tends to develop larger scale structures in the saturated state, which is also shown in this appendix. Most remarkably, at large scale separation, there is the development of a slight dominance of one field component over the other, which can lead to the formation of diagonal structures.

## 5 CONCLUSIONS

It is well known that in virtually all cases of astrophysical interest, Kolmogorov-type turbulence is always accompanied by dynamo action. This has consequences for the way turbulent energy is being dissipated into heat and radiation, which depends strongly on the value of the magnetic Prandtl number (Brandenburg 2014; Brandenburg & Rempel 2019). It is also well known that in the kinematic regime, the small-scale dynamo produces a characteristic spectrum known as the Kazantsev spectrum (Kazantsev 1968), which was later also found and discussed in more detail by Kulsrud & Anderson (1992). The Kazantsev spectrum is now also clearly seen in simulations (Schekochihin et al. 2004; Haugen et al. 2004). Our work has shown that its spectral range is confined to the inertial range of the turbulence and that on larger scales one has a Batchelor spectrum, which turns into a Saffman spectrum as the dynamo saturates.

The Kazantsev spectrum is found to be linked to an excess  $E$  polarization over the  $B$  polarization at subresistive scales, and the opposite trend is found at larger scales. An excess of the  $E$  polarization is observed in the Galactic microwave foreground mission (Planck Collaboration et al. 2016; Caldwell et al. 2017), but here the relevant scales are believed to be much larger than the viscous scales. It is therefore unlikely that this observation bears any relevance on the Kazantsev spectrum, but this is perhaps also because the Kazantsev spectrum is only expected to occur in the kinematic phase. In any case, our numerical findings show that the question of the  $E$  excess is more complicated and that it can depend on a number of unknown factors.

Our study motivates new targets of investigation and new questions. How generic are the different realizations of turbulence found in the present study? Can we really expect the modeled types of velocity and magnetic fields to occur in galaxy clusters or in the ISM? One reason for concern is the fact that in all our flows, the driving is monochromatic with a typical wavenumber  $k_f$ . Real turbulence may be more complicated. Nevertheless, the turbulence should always be characterized by a typical energy-carrying scale,  $\xi_M$ , which defines an approximate position of the spectral peak at  $k_f \approx \xi_M^{-1}$ . It is therefore not obvious, that the monochromatic driving of our turbulence is actually very restrictive.

It is remarkable that the existence of the Kazantsev spectrum appears to be insensitive to the value of the magnetic Prandtl number, but it never occurs at wavenumbers below the turbulent inertial range. Observing the transition to the steeper Batchelor spectrum requires very large domain sizes. This is why we allowed for a forcing scale that was up to 120 times shorter than the size of the domain (Run A). On the other hand, it is conceivable that in real cluster turbulence, the subinertial range is not entirely free of driving, as was assumed in the present work. However, clarifying this observationally could be difficult and may require full-sky observations to be able to identify the true peak of the spectrum.

Real galaxy cluster turbulence is believed to be driven by cluster mergers (e.g., Roettiger et al. 1999), and that the turbulence would be a state of decay in between such mergers events. An open question is therefore whether the Kazantsev spectrum can also be seen in decaying turbulence. There is no reason why not, but it is not easy to find and requires, as we have now seen, a sufficiently extended inertial range. On the other hand, a large magnetic Prandtl number is not required.

Our work has shown that differences between the parity-even  $E$  and the parity-odd  $B$  polarizations may serve to distinguish between Kazantsev and Batchelor spectra. All our runs with noticeable spectral differences between  $E$  and  $B$  had Kazantsev spectra in the iner-



tial range. There were also cases where the PDFs were non-Gaussian with strong skewness in the  $E$  polarization. Subviscous scales played a decisive role in producing excess  $E$  polarization, which might not be observationally accessible. Conversely, of course, if the observed excess  $E$  polarization can only be explained as a subviscous phenomenon, it might just be this effect that would give us information about subviscous scales. Simulations by Kritsuk et al. (2018) also produced excess  $E$  polarization, but the reason behind this was not explained. Those simulations were ideal ones, so the viscous scale was an entirely numerical phenomenon in their simulations. Nevertheless, a detailed spectral analysis might help shedding more light on the phenomenon of excess  $E$  polarization. The strong skewness in the  $E$  polarization during the kinematic regime may have been caused by the elongated structures that are also clearly seen in images of  $E$ , provided  $\text{Pr}_M$  is large. This is expected to be the case in the ISM and in galaxy clusters, which motivates further morphological and statistical studies of observed  $E$  and  $B$  polarizations.

## ACKNOWLEDGEMENTS

This work was supported by the Swedish Research Council (Vetenskapsrådet, 2019-04234). Nordita is sponsored by Nordforsk. We acknowledge the allocation of computing resources provided by the Swedish National Allocations Committee at the Center for Parallel Computers at the Royal Institute of Technology in Stockholm and Linköping.

## DATA AVAILABILITY

The source code used for the simulations of this study, the PENCIL CODE (Pencil Code Collaboration et al. 2021), is freely available on <https://github.com/pencil-code/>. The DOI of the code is <https://doi.org/10.5281/zenodo.2315093>. The simulation setups and the corresponding secondary data, as well as supplemental material with additional plots for the PDFs of Run B and diagnostic images and spectra for Runs B and D in the saturated state are available on <https://doi.org/10.5281/zenodo.6862459>; see also <https://www.nordita.org/~brandenb/projects/Kazantsev-Subinertial> for easier access to the same material as on the Zenodo site.

## REFERENCES

Banerjee R., Jadamzik K., 2004, *PhRvD*, 70, 123003  
 Batchelor G. K., 1950, *Proc. Roy. Soc. Lond. Ser. A*, 201, 405  
 Bhat P., Subramanian K., 2013, *MNRAS*, 429, 2469  
 Boldyrev S., 2005, *ApJL*, 626, L37  
 Boldyrev S., 2006, *PhRvL*, 96, 115002  
 Brandenburg A., 2014, *ApJ*, 791, 12  
 Brandenburg A., 2019, *MNRAS*, 487, 2673  
 Brandenburg A., Boldyrev S., 2020, *ApJ*, 892, 80  
 Brandenburg A., Furuya R. S., 2020, *MNRAS*, 496, 4749  
 Brandenburg A., Kahnishvili T., 2017, *PhRvL*, 118, 055102  
 Brandenburg A., Rempel M., 2019, *ApJ*, 879, 57  
 Brandenburg A., Stepanov R., 2014, *ApJ*, 786, 91  
 Brandenburg A., Enqvist K., Olesen P., 1996, *PhRvD*, 54, 1291  
 Brandenburg A., Kahnishvili T., Tevzadze A. G., 2015, *PhRvL*, 114, 075001  
 Brandenburg A., Kahnishvili T., Mandal S., Pol A. R., Tevzadze A. G., Vachaspati T., 2017, *PhRvD*, 96, 123528  
 Brandenburg A., Haugen N. E. L., Li X.-Y., Subramanian K., 2018, *MNRAS*, 479, 2827

**Table A1.** Values of  $\text{Ma}$ ,  $\tilde{k}_\nu$ , and  $\tilde{\epsilon}_K = \epsilon_K/k_1 c_s^3$  during the kinematic and saturated stages.

Run	Ma	sat.	$\tilde{k}_\nu$	sat.	$\tilde{\epsilon}_K$	saturated
A	0.111	0.102	764	718	$9.2 \times 10^{-3}$	$7.2 \times 10^{-3}$
B	0.121	0.105	389	328	$2.9 \times 10^{-3}$	$1.5 \times 10^{-3}$
C	0.118	...	106	...	$9.9 \times 10^{-4}$	...
D	0.122	0.079	62	50	$4.1 \times 10^{-4}$	$1.7 \times 10^{-4}$
E	0.130	0.096	461	330	$3.6 \times 10^{-4}$	$9.5 \times 10^{-5}$

Brandenburg A., Kahnishvili T., Mandal S., Roper Pol A., Tevzadze A. G., Vachaspati T., 2019a, *PhRvF*, 4, 024608  
 Brandenburg A., Bracco A., Kahnishvili T., Mandal S., Roper Pol A., Petrie G. J. D., Singh N. K., 2019b, *ApJ*, 870, 87  
 Caldwell R. R., Hirata C., Kamionkowski M., 2017, *ApJ*, 839, 91  
 Cho J., Ryu D., 2009, *ApJL*, 705, L90  
 Christensson M., Hindmarsh M., Brandenburg A., 2001, *PhRvE*, 64, 056405  
 Dobler W., Haugen N. E., Yousef T. A., Brandenburg A., 2003, *PhRvE*, 68, 026304  
 Durrer R., Caprini C., 2003, *J. Cosmology Astropart. Phys.*, 2003, 010  
 Falkovich G., 1994, *Physics of Fluids*, 6, 1411  
 Haugen N. E., Brandenburg A., Dobler W., 2004, *PhRvE*, 70, 016308  
 Kamionkowski M., Kosowsky A., Stebbins A., 1997, *PhRvL*, 78, 2058  
 Kazantsev A. P., 1968, *Sov. J. Exp. Theor. Phys.*, 26, 1031  
 Kida S., Yanase S., Mizushima J., 1991, *Physics of Fluids A*, 3, 457  
 Krause F., Rädler K.-H., 1980, *Mean-Field Magnetohydrodynamics and Dynamo Theory*. Pergamon Press (also Akademie-Verlag: Berlin), Oxford  
 Kritsuk A. G., Flauger R., Ustyugov S. D., 2018, *PhRvL*, 121, 021104  
 Kulsrud R. M., Anderson S. W., 1992, *ApJ*, 396, 606  
 Meneguzzi M., Pouquet A., 1989, *J. Fluid Mech.*, 205, 297  
 Meneguzzi M., Frisch U., Pouquet A., 1981, *PhRvL*, 47, 1060  
 Moffatt H. K., 1978, *Magnetic Field Generation in Electrically Conducting Fluids*. Cambridge University Press, Cambridge  
 Nordlund A., Brandenburg A., Jennings R. L., Rieutord M., Ruokolainen J., Stein R. F., Tuominen I., 1992, *ApJ*, 392, 647  
 Olesen P., 1997, *Phys. Lett. B*, 398, 321  
 Pacholczyk A. G., 1970, *Radio astrophysics. Nonthermal processes in galactic and extragalactic sources*  
 Pencil Code Collaboration et al., 2021, *JOSS*, 6, 2807  
 Planck Collaboration et al., 2016, *A&A*, 586, A133  
 Reppin J., Banerjee R., 2017, *PhRvE*, 96, 053105  
 Roettiger K., Stone J. M., Burns J. O., 1999, *ApJ*, 518, 594  
 Saffman P. G., 1967, *J. Fluid Mech.*, 27, 581  
 Schekochihin A. A., 2020, arXiv e-prints, p. arXiv:2010.00699  
 Schekochihin A. A., Cowley S. C., Taylor S. F., Maron J. L., McWilliams J. C., 2004, *ApJ*, 612, 276  
 Seljak U., Zaldarriaga M., 1997, *PhRvL*, 78, 2054  
 Seta A., Federrath C., Livingston J. D., McClure-Griffiths N. M., 2022, arXiv e-prints, p. arXiv:2206.13798  
 Steenbeck M., Krause F., Rädler K. H., 1966, *Zeitschr. Naturf. A*, 21, 369  
 Subramanian K., 2019, *Galaxies*, 7, 47  
 Subramanian K., Brandenburg A., 2014, *MNRAS*, 445, 2930  
 Sur S., Bhat P., Subramanian K., 2018, *MNRAS*, 475, L72

## APPENDIX A: CHANGES DURING SATURATION

As the dynamo saturates,  $u_{\text{rms}}$ ,  $k_\nu$ , and  $\epsilon_K$  decrease by a certain amount that depends on the input parameters. This is demonstrated in Table A1, where we list the kinematic and saturated values for all five runs. We recall that Run C was not continued into saturation, which is here indicated by the ellipses.

Based on the values listed in Table A1, we can infer that the ratios of the saturated to the kinematic values depend either on  $\text{Re}_M$  or on

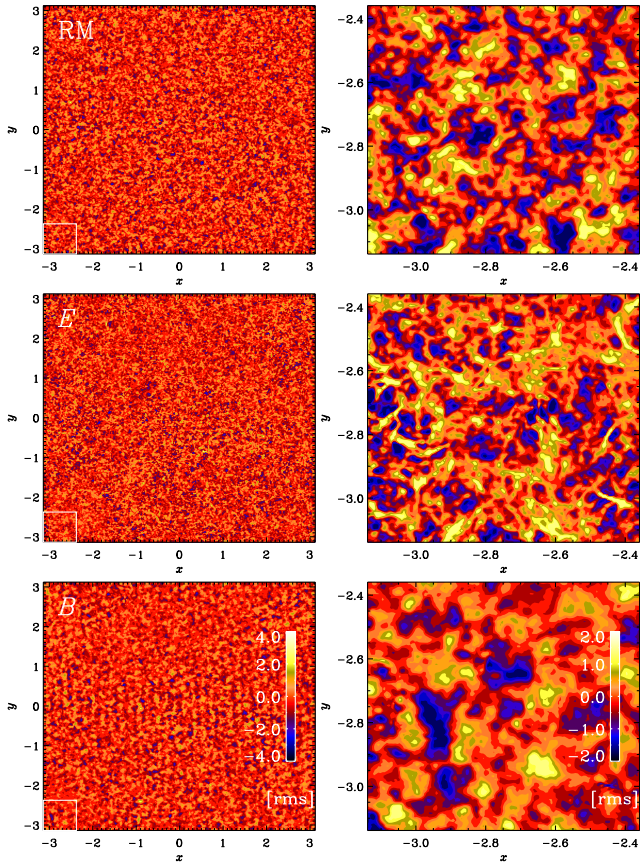


**Figure B1.** Same as Fig. 8, but for Run B during the kinematic stage.

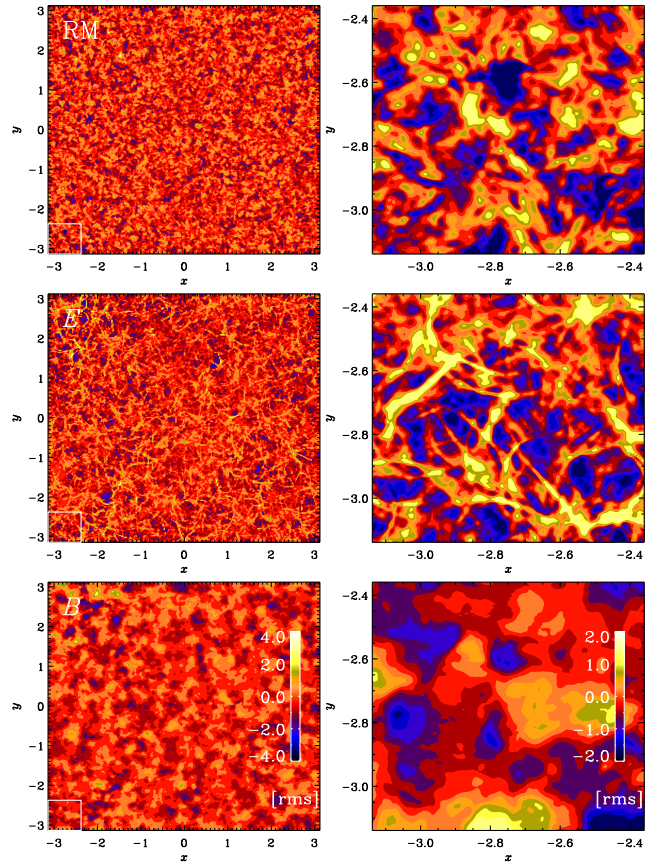


**Figure B3.** Same as Fig. 8, but for Run C during the kinematic stage.

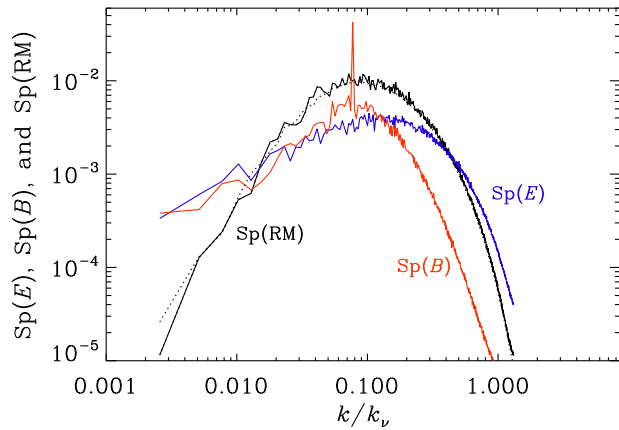


**Figure B2.** Same as Fig. 9, but for Run B during the kinematic stage.

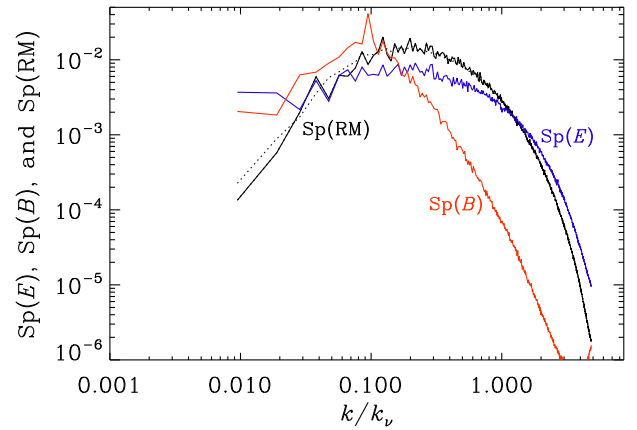


**Figure B4.** Same as Fig. 9, but for Run C during the kinematic stage.

Re. Specifically, we see that  $u_{\text{rms}}(\text{sat})/u_{\text{rms}}(\text{kin})$  decreases mainly with  $\text{Re}_M$  like  $\text{Re}_M^{-0.07}$ ,  $k_\nu(\text{sat})/k_\nu(\text{kin})$  decreases like  $\text{Re}_M^{-0.04}$ , and  $\epsilon_K(\text{sat})/\epsilon_K(\text{kin})$  decreases mainly with Re like  $\text{Re}^{-1/4}$ .

## APPENDIX B: DIAGNOSTICS FOR OTHER RUNS

In Sect. 4.2, we presented diagnostic images and spectra for Runs E, A, and D. Here we also present those for Runs B and C; see Figs. B1–B4. Between Runs B and C, we see a gradual increase in the elongated

structures in  $E$ , which is typical for all runs with  $\text{Pr}_M = 1$ . These are all for the kinematic stage, but in this appendix we also present results for the saturated stage of Runs A and E; see Figs. B5–B8. During saturation, the most remarkable change is seen in the  $B$  polarization of Run A, which consists of stripes that are inclined by  $45^\circ$ . This is caused by a systematic dominance of vertical field components in the saturated state, which causes the formation of stacked clover leaf patches in the  $B$  polarization, as was demonstrated previously in the appendix of Brandenburg & Furuya (2020).



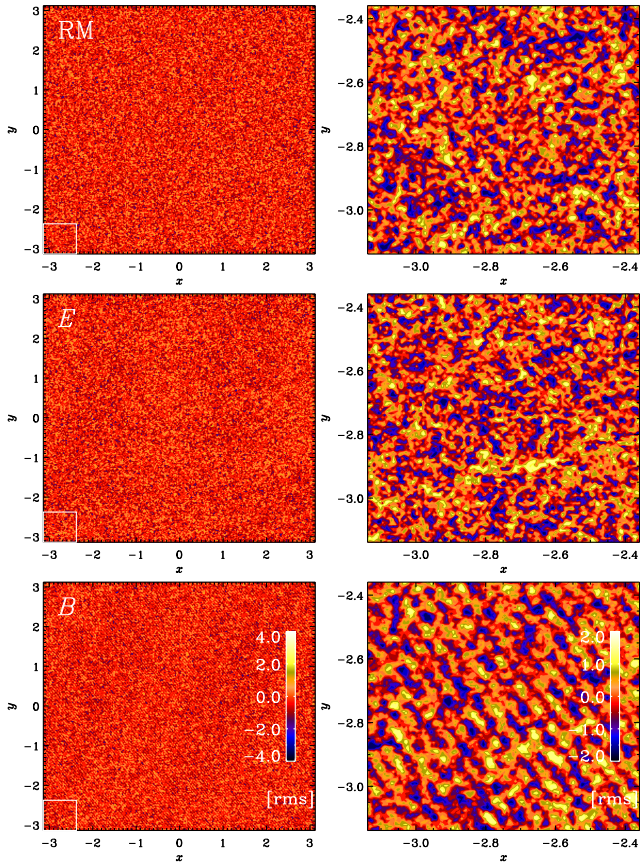


Figure B5. Same as Fig. 8, but for Run A during the saturated stage.

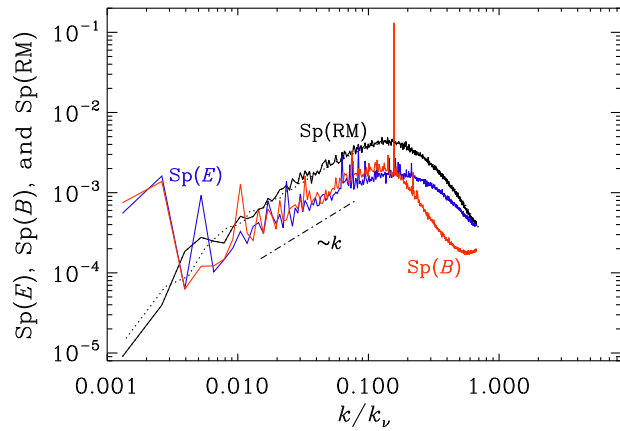


Figure B6. Same as Fig. 9, but for Run A during the saturated stage.

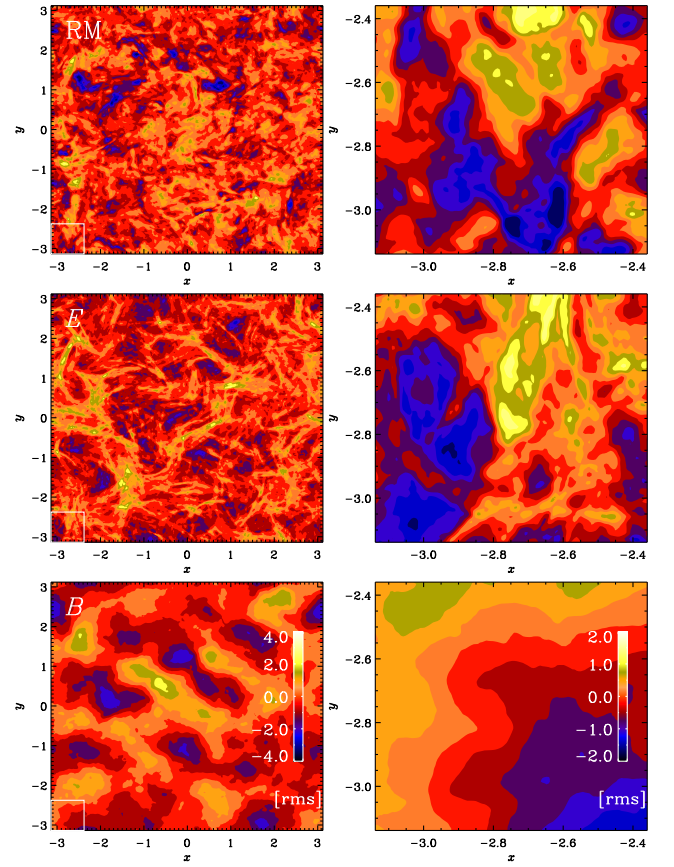


Figure B7. Same as Fig. 8, but for Run E during the saturated stage.

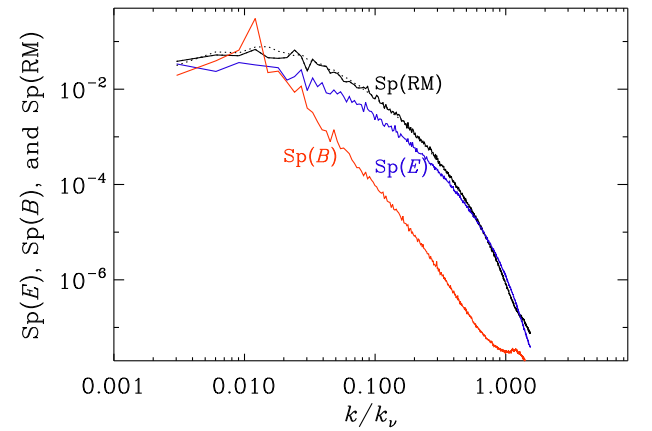


Figure B8. Same as Fig. 9, but for Run E during the saturated stage.

This paper has been typeset from a  $\text{\TeX}/\text{\LaTeX}$  file prepared by the author.